ChemElectroChem

Research Article
doi.org/10.1002/celc.202201070

Chemistry Europe
European Chemical Societies Publishing

www.chemelectrochem.org

Sodium Insertion into $Fe[Fe(CN)_6]$ Framework Prepared by Microwave-Assisted Co-Precipitation

Fabio Maroni[+],[a] Min Li[+],[b] Saustin Dongmo,[a] Cornelius Gauckler,[a] Margret Wohlfahrt-Mehrens,[a, c] Marco Giorgetti,[b] and Mario Marinaro*[a]

Prussian blue analogues (PBAs) are interesting materials for Na electrochemical insertion, owing to their ease of synthesis, rigid open framework and large interstitial space. In this work, iron hexacyanoferrate nanoparticles, $Fe^{III}[Fe^{III}(CN)_6]$, also known as Berlin green (BG), where both Fe centers are in the Fe(III) configuration, have been synthesized by an easy microwave assisted co-precipitation method, with an average particle size of around 44 nm. The BG nanoparticles exhibited a 120 mAh g^{-1} specific capacity with a capacity retention of 84.8% over 100 cycles at 20 mA g^{-1} current and up to 80 mAh g^{-1} at 10 C rate. The initial charge and discharge processes were fully investigated by ex-situ X-ray absorption spectroscopy (XAS). The XAS results reveal that there is some irreversibility in the initial electrochemical processes and the Fe–C and Fe–N bond lengths change during the first charge/discharge cycle. This effect was attributed to BG electrode activation processes, and partly explained the observed capacity fading.

Introduction

Current wide deployment of renewable energy sources (RESs) has highlighted the necessity of effective stationary energy storage devices to balance grid fluctuations, due to the intermittent nature of RESs. Electrochemical energy storage systems play a fundamental role in both stationary and mobile applications. Since their commercialization in the early 1990s, Lithium-ion Batteries (LIBs)[1] have become the most widespread energy storage technology due to their high-energy density and high performance, which are desirable for modern storage applications. Despite these premises, LIBs still suffer from several drawbacks which do not allow them to be a one-for-all solution in all technical scenarios: raw materials supply bottlenecks, safety issues and the lack of a real circular economy around them.[2] For these reasons, a series of new chemistries have been attracting more and more attention in last few years, as potential future alternatives, the so-called post-lithium systems.[3,4] Among them, while on the one hand the monovalent Na-ion batteries (NIBs) seem to be promising[5] and closer to a mass-market debut, multivalent ion batteries such as Magnesium-ion (MIBs) and Calcium-ion (CIBs) systems, are still in their infancy despite a greatly renewed interest, surfaced in the last two decades.[6]

NIBs can benefit from a ready and relatively rapid technology transfer from LIB technology. In this regard, the quest for low-cost, easy-to-synthesize and high performance cathode materials is restless.[7,8] Among all the already known materials, Prussian blue analogs (PBAs), with the general formula $A_xM'[M''(CN)_6]_{1-y}\square_y \cdot zH_2O$, where A ($0 \le x \le 2$) represents the inserted cation (A = Na^+, K^+, Ca^{2+}, Zn^{2+}), M' and M'' are the transition metals (TMs), $\square$ refers to $M''(CN)_6$ vacancies ($0 \le y \le 1$), the H_2O content includes both interstitial and crystallization water molecules,[9] have been investigated as cathodes in both aqueous and non-aqueous electrolytes for Li^+ ($r = 0.76$ Å), Na^+ ($r = 1.02$ Å), Ca^{2+} ($r = 1.02$ Å), K^+ ($r = 1.52$ Å) and Zn^{2+} ($r = 0.74$ Å) ion batteries,[10–15] owing to their 3D open framework, large interstitial space, and abundant redox-active sites.[16] Iron hexacyanoferrate or Prussian blue, $A_xFe[Fe(CN)_6]$ or PB, as predecessor of hexacyanometallates, has been widely investigated as Na^+ insertion material, due to the cheap and abundant Fe as active redox center, high theoretical capacity against Na^+ insertion (theoretical two-electron transfer process) and ease of preparation. The most commonly used method for the bulk synthesis of PBAs is a simple co-precipitation, which actually leads to a hydrated PBA lattice with large amounts of $Fe(CN)_6$ vacancies and coordinated water. The presence of $Fe(CN)_6$ vacancies and coordinated water in lattice causes a variety of adverse effect that can severely deteriorate the electrochemical performance of PBAs framework.[17,18] In order to solve these problems, various synthesis strategies have been reported to minimize the content of the lattice vacancies and water, and to improve the crystallinity of PBA materials. For example, by synthesizing high phase purity and lattice-perfect single crystal PB nanoparticles,[19] or preparing high-quality PB

[a] Dr. F. Maroni,[+] Dr. S. Dongmo, C. Gauckler, Dr. M. Wohlfahrt-Mehrens, Dr. M. Marinaro
Zentrum Für Sonnenenergie Und Wasserstoff Forschung Baden-Württemberg (ZSW)
Helmholtzstraße 8, 89081, Ulm (Germany)
E-mail: mario.marinaro@zsw-bw.de
[b] M. Li,[+] Prof. M. Giorgetti
Department of Industrial Chemistry "Toso Montanari
University of Bologna
Viale del Risorgimento 4,I-40136 Bologna (Italy)
[c] Dr. M. Wohlfahrt-Mehrens
Helmholtz Institute Ulm (HIU) Electrochemical Energy Storage
Helmholtz Str. 11, D-89081 Ulm (Germany)
[+] These authors contributed equally to the work.

Supporting information for this article is available on the WWW under https://doi.org/10.1002/celc.202201070

compounds by controlling the precursor concentration, careful control of the synthesis temperature, or by adding chelating agents or surfactants.[20–23] –

In the last few years, microwave reactors emerged as a fast, precise and effective way to synthesize high quality nanoparticles. Microwave processing allows for a fast and uniform heating of the precursor solutions, favoring nucleation processes that lead to the formation of small crystallites.[24] It has also been employed in the preparation of battery materials with success.[25–29]

In this work, iron hexacyanoferrate nanoparticles, $Fe^{III}[Fe^{III}(CN)_6]$, also known as Berlin green (BG),[30] were synthesized by combining both co-precipitation and microwave irradiation methods, with an average particle size in the sub-100 nm range. The BG material has been fully characterized, its electrochemical Na^+ insertion capabilities were investigated and a full set of ex-situ X-ray absorption (XAS) experiments has been employed to highlight the influence of the initial Na^+ insertion/extraction processes on the BG electron structure and bond lengths.

Results and Discussion

The detail of the hexacyanoferrate preparation procedure is reported in Scheme 1. The process is straightforward and does not include any complicate synthesis step. The precursor 0.1 M solution of $K_3Fe(CN)_6$ is added dropwise to the 0.1 M solution of $FeCl_3$, while keeping the system under stirring, at room temperature.

The color quickly changes from pale yellow to a yellow-tinted dark green color, with the formation of a colloidal solution. Then, the as obtained colloid was transferred in batches into rubber-sealed glass vials and put into the microwave reactor, where the 60 °C target temperature was kept for 6 hours. Post-synthesis step included centrifugation, washing two times with H_2O and acetone and then a drying step under vacuum at 60 °C for 6 hours to reduce the interstitial H_2O content, thus obtaining the final product. ICP analysis excluded the presence of any foreign metal cation in the BG material, in particular, K^+ from the $K_3Fe(CN)_6$ precursor.

The crystal structure of the resulting BG material was investigated by means of X-ray diffraction (XRD), which is shown in Figure 1a. The XRD pattern of BG fits very well with the PDF database card available for hexacyanoferrate species (PDF 00-052-1907) and it could be indexed with a cubic phase

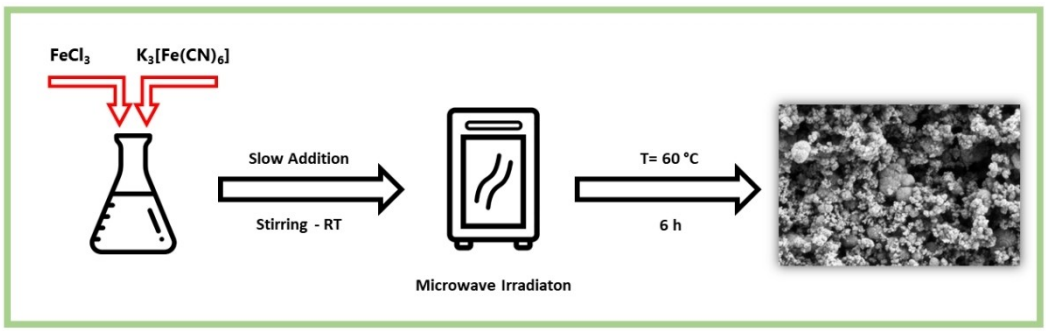

Scheme 1. Preparation procedure of the Iron Hexacyanoferrate material.

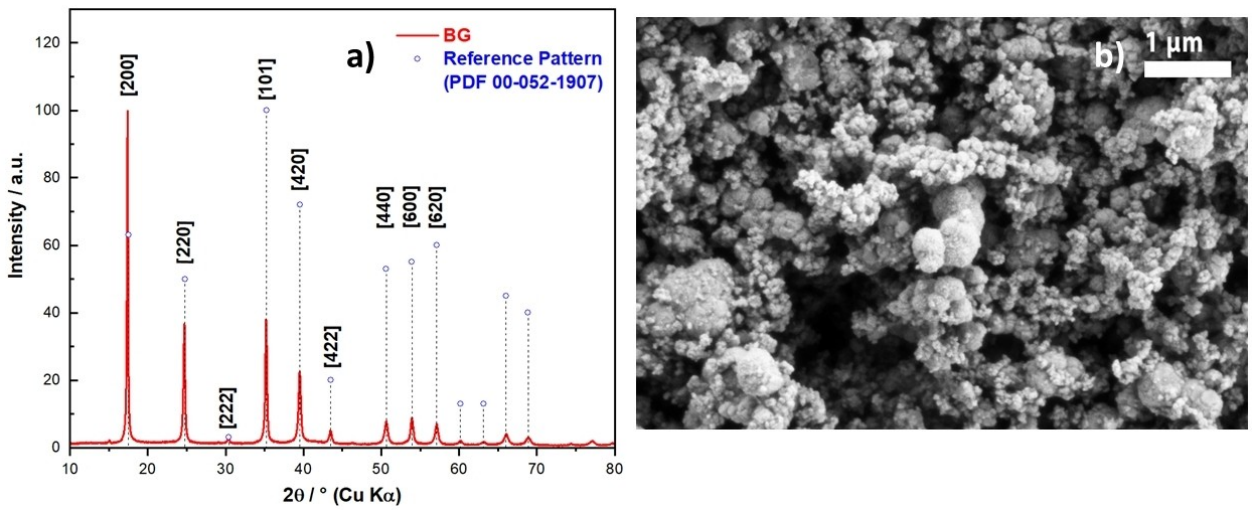

Figure 1. XRD pattern (a) and SEM micrograph (b) of the Berlin green (BG).

(*Fm3 m* space group). High resolution powder X-ray diffraction patterns were acquired and refined (a = 10.2045 (4) Å) in order to calculate the $[Fe(CN_6)]^{3-}$ vacancy content in the structure, which resulted to be 0.262(10). Refinement data is shown in Figure S1 and Table S1. The cubic structure is characterized by octahedrally coordinated transition metal ions, bridged by C≡N ligands: one of the Fe^{3+} sites is bonded to C atoms, and the other Fe^{3+} is coordinated to N atoms. Due to the different crystal field stabilization energy,[31] the TM ions present in the structure display a different splitting of the 3d orbitals, which ends in different spin states for the two Fe sites, namely Fe^{HS} (High Spin)–N and Fe^{LS} (Low Spin)–C. These differences in spin states determine the electrochemical behavior of the Fe-sites in two different potential areas and will be discussed in the next paragraphs.

Figure S2 shows the normalized FTIR spectra of the as-synthesized BG powder and pristine electrode. The two spectra show a good overlap with the main band (≈2200 cm^{-1}–2050 cm^{-1}) assigned to the stretching mode of the ν(C≡N) bond. The peak results to be split in a main feature located at 2040 cm^{-1}–2067 cm^{-1} and a smaller band at 2169 cm^{-1}–2158 cm^{-1}. In the pristine state, the less intense bands were assigned to ν(O–H) bond stretching and ν(H–O–H) bond bending are located at 3318 cm^{-1} and 1604 cm^{-1}, respectively. The peak split of the –C≡N– bond is in line with literature reports on the oxidation state of the hexacyanoferrate, corresponding to that of the (BG) PBA.[32]

In Figure 1b, SEM micrographs show the morphology of the BG material, which is mainly composed of homogenous and well distributed small primary spherical crystallites, which slightly agglomerated into secondary units in the hundreds of nanometers size range.

The average crystallite size has been estimated with the Scherrer equation[33], shown in Equation (1):

$$\tau = \frac{K\lambda}{\beta \cos\theta} \quad (1)$$

where K is the so-called shape factor (≈0.9), λ is the wavelength of the incident radiation (Cu Kα = 1.5401 Å), β is the peak widening at FWHM (in radians) and θ is the Bragg angle of the peak taken into consideration for the size estimation. The estimation was based on the [200] reflection and the obtained value is an average crystallite size of 44 nm. To further confirm the absence of any kind of intercalant ion and/or contaminants in the PBA material, EDX spectra analysis were recorded for the pristine powder sample, as shown in Figure S3. It can be clearly seen that only relevant C, N and Fe, signals are observed, testifying the high purity of the obtained product.

Thermogravimetric analysis was used to determine H_2O content, which is one of the most important parameters that determine the final electrochemical performance of any PBA material.[34] The results of the analysis are shown in Figure S4. In this case, the BG material showed a weight loss of 15.59% at ≈160 °C, which corresponds to ≈2.8 molecules of water. Therefore, final formula can be written as $Fe[Fe(CN)_6]_{0.738}{*}2.8H_2O$.

Figure 2 displays the cyclic voltammogram of the BG electrode carried out at scan rate of 0.050 mV s^{-1}. BG show two well separated redox signals in their respective potential range, which is accordance to two different spin states of the two Fe atoms, one linked to the carbon of the cyanide, Fe^{III}–C (low spin, ls), the other to the nitrogen, Fe^{III}–N (high spin, hs). This is caused by the Fe 3d orbital splitting triggering the Fe atoms to be in different spin states. Because of the strong ligand field of

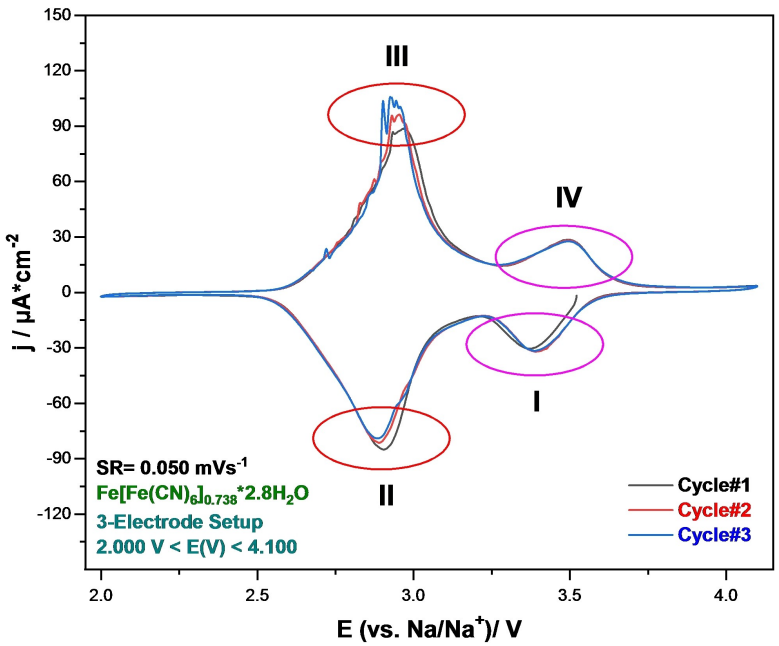

Figure 2. BG cyclic voltammetry experiment. Scan Rate = 0.050 mV s^{-1}. Experiment conducted at room temperature.

the cyanide, the Fe coordinating C always adopts a low spin configuration, while the opposite is true for the N-coordinated Fe, where a high spin state is observed.[35] It is therefore possible to summarize the activity of an ideal BG with the following electrochemical reactions, considering as reference a monovalent cation, with an ideal stoichiometry of 2 A^+ inserted cations and no vacancies. A two steps electrochemical reaction is taking place during the discharge (forward) and charge (reverse) processes, with Equation (2) due to the Fe^{III}–C(ls) redox couple and Equation (3) to the Fe^{III}–N(hs) redox couple, respectively.

$$Fe^{3+}\ Fe^{3+}(CN)_6 \cdot zH_2O + A^+ \leftrightarrows AFe^{3+}\ Fe^{2+}(CN)_6 \cdot zH_2O \quad (2)$$

$$Fe^{3+}\ Fe^{2+}(CN)_6 \cdot zH_2O + A^+ \leftrightarrows A_2Fe^{2+}\ Fe^{2+}(CN)_6 \cdot zH_2O \quad (3)$$

Figure 2 well agrees with the above statement showing two electrochemical couples indicated by I–IV and II–III, respectively. The I–IV couple, assigned to the low spin iron Fe^{III}–C(ls), is located at $E = 3.39$ V (I – vs. Na/Na^+) in the cathodic area, and $E = 3.49$ V (IV – vs. Na/Na^+) in the anodic area, respectively. The II–III couple, assigned to the high-spin iron Fe^{III}–N(hs), is characterized by a couple of peaks at $E = 2.89$ V (II – vs. Na/Na^+) in the cathodic area and an anodic peak at $E = 2.94$ V (III – vs. Na/Na^+).[19]

Galvanostatic charge/discharge performance was investigated at room temperature (Figure 3 and Figure S5). The BG shows a first cycle discharge capacity of 120 mAh g^{-1} and a good reversibility, with 84.8% capacity retention after 100 cycles ($I = 20$ mA g^{-1}). Selected galvanostatic profiles (cycles 1, 5, 10, 20 and 50) are depicted in Figure 3b: the discharge profiles are characterized by two sloping plateau regions in the $E =$ 3.70 V–$E = 3.34$ V (vs. Na/Na^+) range, assigned to the reduction of Fe^{III}–C(ls) atom and in the $E = 3.00$ V–$E = 2.64$ V (vs. Na/Na^+), assigned to the reduction of Fe^{III}–N(hs) atom. Differential analysis of selected cycles (Figure S5) showed consistent behavior with CV data.

Figure S6 and Table S2 show the rate capability results of the BG-electrodes, carried out with a reference specific current of I(1 C) = 120 mA g^{-1}. The BG electrodes showed a very good kinetic response up to 10 C rate ($I = 1200$ mA g^{-1}), with specific capacities ranging from 138 mAh g^{-1} (C/20) to 80 mAh g^{-1} at 10 C rate. The degree of polarization was small, with respect to increasing rates, as can be seen from the specific capacity profiles showed in Figure S7a. As showed in Figure S7b, differential analysis helped to investigate the BG response to higher cycling rates, confirming the relatively limited polarization, ranging from $I = 6$ mA g^{-1} to $I = 1200$ mA g^{-1}. This kinetic behavior is consistent with literature data and can be assigned to the open cubic framework structure with large sites, and the presence of H_2O molecules that partially shield the Na^+ charge, thus decreasing the degree of electrostatic interactions with the host structure and favoring faster diffusion.[10]

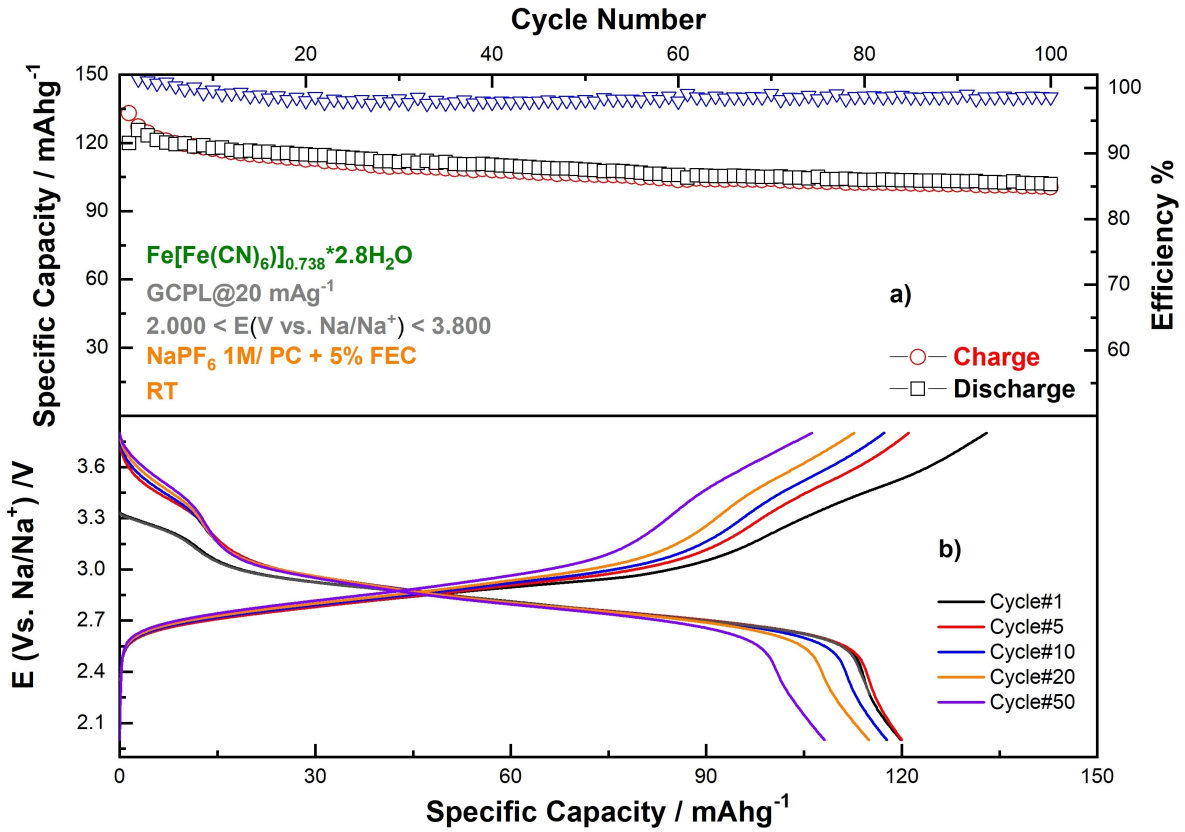

Figure 3. Galvanostatic cycling experiment for BG at $I = 20$ mA g^{-1} in the 2.00 V < E (vs. Na/Na^+) < 3.80 V range. Specific capacity vs. cycle number (a) and voltage vs capacity profiles (b). Experiments conducted at RT.

Given this good kinetic response, to further investigate and partially quantify the transport properties of the material at a given potential value, a galvanostatic intermittent titration experiment (GITT) was used. This electrochemical technique has largely proven its reliability since its introduction. In addition, to maximize experimental reliability, the GITT was carried out in a 3-electrode cell setup to carefully monitor the working electrode (WE) potential.

The GITT[36] experiment (Figure 4) was conducted using a C/80 rate current pulse of 1 h duration, followed by a variable cell relaxation time, defined by a limit 5 mV h^{-1} voltage variation, to ensure the same conditions for all the pulses. The apparent diffusion coefficient D_{App} was calculated according to Equation (4):

$$DApp = \frac{4}{\pi\tau}\left(\frac{m_B V_m}{M_B S}\right)^2\left(\frac{\Delta E_s}{\Delta E_\tau}\right)^2 \quad (4)$$

Where τ is the pulse duration in s, m_B is the mass of the active material on the electrode, V_m is the molar volume in cm^3 mol^{-1}, M_B is the molecular weight of the BG species in g mol^{-1}, S is the geometrical surface of the electrode, ΔE_s is the relaxation potential variation and ΔE_τ is the potential variation within a current pulse. The D_{App} vs. E(V) plot shows a quite stable value, with 10^{-9} cm^2 s^{-1} order of magnitude throughout the experiment, in which Na^+ ions were inserted into BG. The drop *in* D_{App} values at $\approx E = 2.660$ V (vs. Na/Na^+) is consistent with the end of the insertion step and the capacity profile slope variation like showed in Figure 3.

X-ray absorption spectroscopy study

The electrochemical performance of electrode materials derive from the combination of both structural and electronic properties and their reversible evolution during charge and discharge processes.[11] The structural and electronic modification of Fe sites upon Na^+ insertion/extraction was therefore here investigated by means of ex-situ X-ray absorption (XAS) at the K-edge of Fe, on pristine, fully discharged and charged electrodes. X-ray absorption spectroscopy (XAS), as element-specific characteristic technique, can provide both chemical and structural information at the same time.[37,38] Here, electrodes discharged to $E = 2.00$ V (vs. Na^+/Na) and charged to $E = 3.80$ V (vs. Na^+/Na) respectively, were used to probe induced variations on characteristic first shell bond distances at the Fe sites and on the Fe oxidation states upon Na^+ full insertion and full release.

As observed in Figure 5a, XANES spectra are characterized by a pre-edge region A, which is due to the transition to bound states (the 1*s*–3*d* transition). The rising portion of XANES (labeled as B) is the "edge region", and the main peak (labeled as C) is called the "edge resonance". Edge resonance is associated to the continuum and involves multiple scattering resonances of the photoelectrons.[39] Thus, the evolution of Fe K-edge XANES indicates a change of both oxidation states and electronic arrangements of Fe-sites. After the first discharge, the Na-ions were inserted into the BG structure. In order to keep the neutrality of the system, the oxidation state of Fe-sites was reduced to Fe^{II}, as it is displayed in Figure 5a. The edge of discharged electrode shifted to the lower energy part, of about 2 eV. This Fe reduction refers to both Fe–C(ls) and Fe–N(hs) as

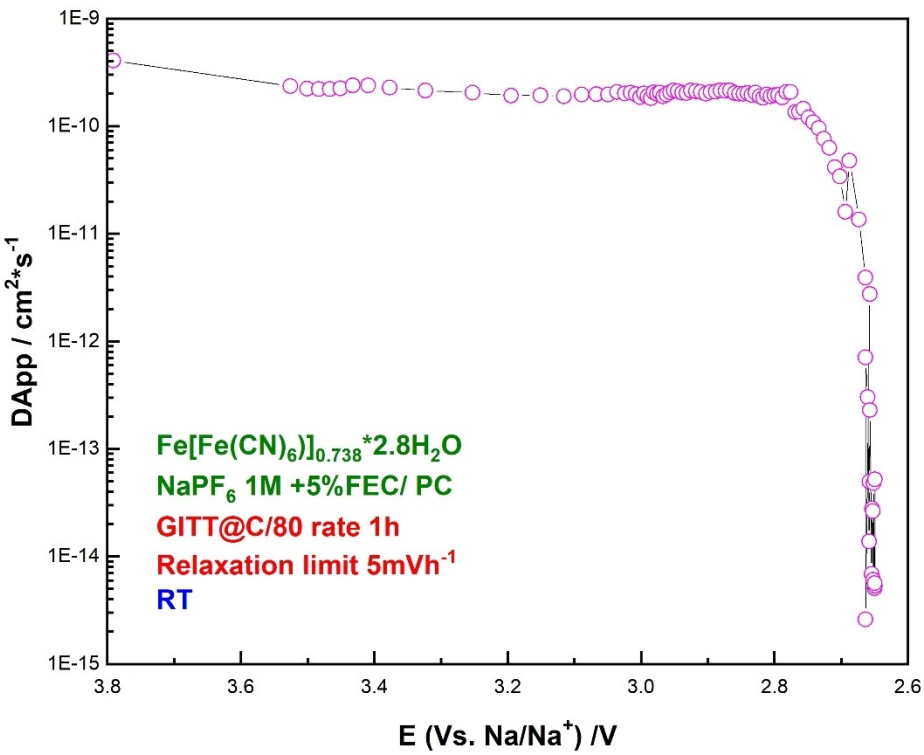

Figure 4. BG GITT experiment: C/80 Current Pulse, 5 mV h^{-1} relaxation condition, room temperature.

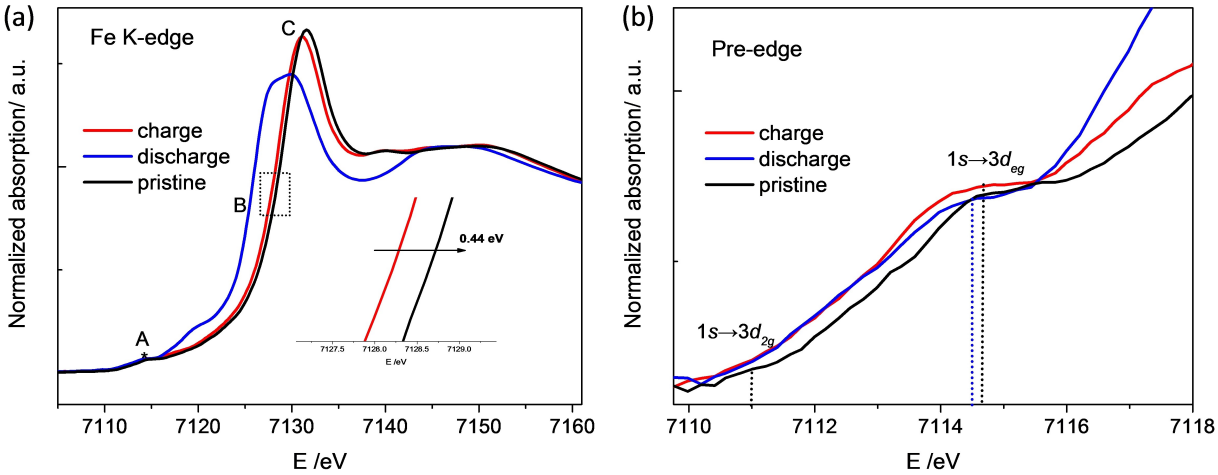

Figure 5. Ex-situ XANES (a) and pre-edge peaks (b) analysis of the Fe K-edge for BG electrodes.

the reduced sample is being reduced to $E = 2.00$ V vs. Na^+/Na. During the subsequent charge process, the edge curve moved back to the higher energy part, which corresponds to the oxidation of both Fe sites to 3+, therefore confirming that the bulk of the material follows a reduction/oxidation phenomenon of Fe centers, as highlighted by the CV testing. Compared to the pristine electrode XANES curve, they are quite close, but not totally restored, which indicates that there might be a small structural activation.

Figure 5b display a magnification of the pre-edge region for all electrodes. The $1s \rightarrow 3d$ transition formally is electric dipole forbidden, but quadrupole allowed. However, an hybridization of metal 4*p* and 3*d* orbitals provide some electric dipole-allowed $s \rightarrow p$ characteristic, thus adding additional intensity to the quadrupole mechanism.[40] The pre-edge spectra of BG electrodes are characterized by a small feature at around 7111 eV and one peak at around 7014.5 eV, due to the $1s \rightarrow 3dt_{2g}$ and $1s \rightarrow 3d_{eg}$ transitions, respectively. This last feature can be used to additionally monitor the Fe oxidation state variation during discharge and charge. The energy of the $1s \rightarrow 3d_{eg}$ transition shifts slightly to lower and higher energy (between the dash lines) accordingly to discharged and charged states.

Additional structural information can be gained by properly analyzing the extended portion of the X-ray absorption spectrum, in all the three electrodes, (pristine, reduced, and the oxidized). Details on this investigation, where the occurrence of strong multiple scattering contributions of the typical linear Fe–C–N–Fe chain, must use the prescription for a correct extraction and interpretation of the EXAFS spectrum in this class of samples, reported recently,[41] and are available as SI. Figure 6 shows the comparison of the experimental (–) and theoretical (…) K^{2-} extracted EXAFS signals for the three electrodes investigated, BG in the pristine state, and in the reduced and oxidized states, and the Table 1 reports the EXAFS refined parameters. It is seen that the theoretical curves match extremely well the experimental ones in all panels, demonstrating the reliability of the present data analysis and of the structural model used.

From a local structural viewpoint, for the Fe site, the bond lengths of Fe–C(Is) and C≡N are kept almost same in the three

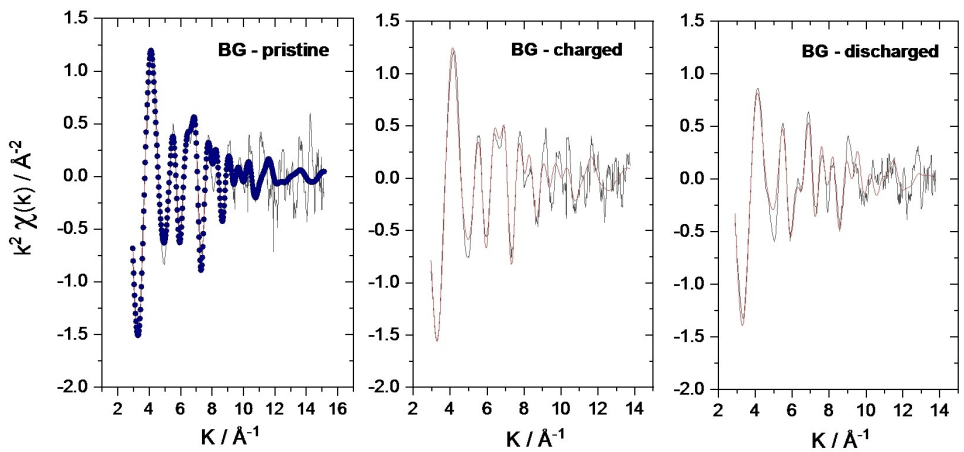

Figure 6. EXAFS Fe K-edge refinement of the BG, pristine, reduced and oxidized electrodes.

Table 1. Relevant EXAFS refined parameters for the studied Berlin green samples. Errors in parenthesis have been evaluated using contour plots (see Figure S7).

	BG	BG – 1 st discharge	BG – 1 st charge
Fe–C [Å]	1.871(8)	1.877(8)	1.869(7)
σ^2 Fe–C [Å^2]	0.008(2)	0.0045(15)	0.0055(15)
C≡N [Å]	1.170(5)	1.17(1)	1.171(5)
σ^2 ≡N [Å^2]	0.010(3)	0.006(2)	0.009(2)
Fe–N [Å]	2.031(8)	2.074(8)	2.030(6)
σ^2 Mn–N [Å^2]	0.0044(15)	0.007(2)	0.0025(10)
θ Fe–C–N [deg]	180 FIX	180 FIX	180 FIX
θ Mn–N–C [deg]	180 FIX	180 FIX	180 FIX
E_0 Fe	7123.5(5)	7121.6(6)	7123.1(5)
S_0^2 Fe	0.88(6)	0.81(5)	0.89(6)
χ^2-like residual (10^{-6})	2.75	1.23	2.84

electrodes investigated. Therefore, the Fe–C local structure is not altered, confirming the low spin state regardless the oxidation state, as expected from the strong ligand field of the cyanide group. On the other hand, the Fe–N (hs) bond length increases appreciably in the reduced state, from 2.031(8) to 2.074(8) Å, but far from the 1.92–1.93 Å value, which is required for a spin crossover, i.e., an Fe–N in the low spin state.[31] Therefore, we can consider that Fe–N do not change spin state during discharge, but still the reduction of the Fe(III)–N to Fe(II)–N slightly influences the first shell structure.

On the one hand, EXAFS analysis has identified in the Fe–N (hs) a local structural variation between the charged and discharged state. On the other hand, the Fe–C (Fe in the low spin state) site is retained upon oxidation/reduction phenomena. The question could be whether this observed Fe(hs)–N bond length elongation/contraction during the first cycle could be sustained for long term cycling. This is out of the aim of the present work and a long term X-ray analysis is currently under investigation.

Conclusions

An iron hexacyanoferrate species was synthesized using an innovative microwave co-precipitation method. This method allowed obtaining very small crystalline particles, with an average size of 44 nm. Electrochemical characterization showed a multi-step electrochemical mechanism, consistently with the presence of Fe atoms in different spin states. Galvanostatic cycling highlighted good electrochemical performances, with a first discharge capacity of 120 mAh g^{-1} at specific current of 20 mA g^{-1} and a capacity retention of 84.8% after 100 cycles. Differential analysis showed a consistent behavior with respect to cyclic voltammetry experiments, and rate capability experiments showed a good performance up to specific currents of $I = 1200$ mA g^{-1}. Transport properties investigation carried out by means of GITT, showed an almost constant value of the apparent diffusion coefficient throughout the Na^+ insertion process. The structural and electronic modifications of Fe sites during the first charge and discharge steps were investigated by means of ex-situ X-ray absorption (XAS) techniques. XANES data showed a consistent reduction and oxidation of the Fe center in the full volume of the electrode upon reduction and oxidation steps. EXAFS data showed that the bond distance of Fe–C and C≡N remained roughly constant during the first cycle. Unlike the Fe–C bond, the Fe–N bond length exhibited appreciable increase during the first discharge process, from 2.031(8) to 2.074(8) Å, which might be the cause of some irreversibility in the system during the long-term electrochemical cycling.

Experimental Section

Materials preparation

The $FeFe(CN)_6$ nanoparticles were prepared by a straightforward microwave-assisted co-precipitation method. In a typical preparation procedure, a 0.1 M aqueous solution of $K_3Fe(CN)_6$ (Sigma-Aldrich) was slowly added to a 0.1 M solution of $FeCl_3$ (Sigma-Aldrich) and transferred to a sealed glass vial equipped a one-way rubber septum. The solution-containing vial was then transferred into a Monowave 400 (Anton Paar®) microwave apparatus, with a target temperature of 60 °C, for 6 hours. The obtained suspension was centrifuged and washed two times with distilled H_2O and acetone, respectively. After room temperature drying, the obtained dark green powder was additionally dried at 60 °C under vacuum for 6 hours.

Materials characterization

Standard XRD patterns were recorded on a Bruker D8-Advance instrument, equipped with a Cu source ($\lambda = 1.5406$ Å), in Bragg-Brentano geometry in the 10°–80° 2θ range. SEM/EDX measurements were carried out on a ZEISS Merlin high-resolution Field Emission electron microscope (FE-SEM), equipped with a X–MAX EDS detector (Oxford Instruments). Thermogravimetric (TGA) measurements for the assessment of the carbon content were carried out in a TA Instruments TGA-5500 instrument in air atmosphere from room temperature to 600 °C at a 5 °C min^{-1} heating rate.

Cell assembly and electrodes preparation

The electrochemical measurements were carried out in 3-electrode Swagelok-type cells. Working electrodes (WEs) were prepared by mixing the active material powder, Super C45 conductive additive (TIMCAL®) and PVdF (Solvay® Solef 5130) in a 70:20:10 ratio. The powders were mixed with N-Methyl-2-pyrrolidinone (NMP) (Sigma Aldrich® – Anhydrous 99.5%) in a ball mill at 200 rpms for 1 h, using rotation/pause steps. Slurries were casted on Al foil (10 μm) at a 150 μmwet thickness and dried at 60 °C for 2 h. Electrode active material mass loading resulted to be ≈1 mg cm^{-2}. All the obtained electrodes were punched out and dried at 120 °C for 12 h before being transferred to an Ar filled glovebox (M-Braun®). A 1 M $NaPF_6$ +5% FEC in propylene carbonate (PC) electrolyte solution was used with Na metal CE and QREs, respectively. Glass fiber separators (Whatman® GF/A) were used in all systems.

Electrochemical measurements

All electrochemical experiments were carried out on a VMP (Bio-Logic®) electrochemical workstation. Cyclic voltammetry (CV) measurements of the active materials were conducted at 0.050 $mV\,s^{-1}$ scan rate in the potential region $2.000\ V < E$ (vs. Na/Na^+) < 3.800 V. All the investigations were conducted at room temperature.

High resolution powder X-ray diffraction

High resolution powder X-ray diffraction (PXRD) data was recorded by using a monochromatic X-ray beam (Wavelength: 0.8266 Å, X-ray Energy: 15.00 keV) at the MCX beamline, Elettra synchrotron in Trieste (Italy). Powder data was collected using capillary geometry, setting the spinner at 3000 rpm. The X-ray diffraction pattern was collected consecutively in the range of $5^\circ < 2\theta < 60^\circ$, with 0.01° steps and an acquisition time of 1 s per step. The crystal structure was refined using GSAS-II software.[42]

X-ray absorption spectroscopy

X-ray absorption spectroscopy (XAS) experiments were conducted at Elettra synchrotron Trieste (Italy), at XAFS beamline.[43] The storage ring was operated at 2.0 GeV in top-up mode with a typical current 300 mA. Data were recorded at Fe K-edge in transmission mode using ionization chambers filled with a mixture of Ar, N_2, and He to have 10%, 70%, and 95% of absorption in the I_0, I_1 and I_2 chambers, respectively. An internal reference of iron foil was used for energy calibration in each scan. This allowed a continuous monitoring of the energy during consecutive scans. The white beam was monochromatized using a fixed exit monochromator equipped with a pair of Si (111) crystals. Spectra were collected with a constant k-step of 0.3 nm^{-1} with 3 s per point acquisition time from 6920 to 8350 eV around Fe K-edge. The extended X-ray absorption fine structure (EXAFS) analysis was performed using the GNXAS package,[44] which is based on the multiple scattering (MS) theory. The method uses the decomposition of the EXAFS signals into a sum of several contributions, namely the n-body terms. The theoretical signal is calculated ab-initio and contains the relevant two-body $\gamma(2)$, three-body $\gamma(3)$, and four-body $\gamma(4)$ MS terms.[45] More details are available in the Supplementary Information.

Acknowledgements

This work contributes to the research performed at CELEST (Center for Electrochemical Energy Storage Ulm-Karlsruhe) and was funded by the German Research Foundation (DFG) under Project ID 390874152 (POLiS Cluster of Excellence). Dr. Giuliana Aquilanti is kindly acknowledged for recording XAS measurements at ELETTRA.

Conflict of Interest

The authors declare no conflict of interest.

Data Availability Statement

The data that support the findings of this study are available from the corresponding author upon reasonable request.

Keywords: Berlin green · Insertion · Prussian blue analogs · Batteries · X-ray absorption spectroscopy

[1] M. V. Reddy, A. Mauger, C. M. Julien, A. Paolella, K. Zaghib, *Materials* **2020**, *13*, 1884.
[2] H. E. Melin, M. A. Rajaeifar, A. Y. Ku, A. Kendall, G. Harper, O. Heidrich, *Science* **2021**, *373*, 384.
[3] Y. Tian, G. Zeng, A. Rutt, T. Shi, H. Kim, J. Wang, J. Koettgen, Y. Sun, B. Ouyang, T. Chen et al., *Chem. Rev.* **2021**, *121*, 1623.
[4] F. Maroni, S. Dongmo, C. Gauckler, M. Marinaro, M. Wohlfahrt-Mehrens, *Batteries & Supercaps* **2021**, *4*, 1221.
[5] C. Delmas, *Adv. Energy Mater.* **2018**, *8*, 1703137.
[6] A. Ponrouch, J. Bitenc, R. Dominko, N. Lindahl, P. Johansson, M. R. Palacin, *Energy Storage Mater.* **2019**, *20*, 253.
[7] I. Hasa, S. Mariyappan, D. Saurel, P. Adelhelm, A. Y. Koposov, C. Masquelier, L. Croguennec, M. Casas-Cabanas, *J. Power Sources* **2021**, *482*, 228872.
[8] C. Gauckler, M. Dillenz, F. Maroni, L. F. Pfeiffer, J. Biskupek, M. Sotoudeh, Q. Fu, U. Kaiser, S. Dsoke, H. Euchner, P. Axmann, M. Wohlfahrt-Mehrens, A. Groß, M. Marinaro, *ACS Appl. Energ. Mater.* **2022**.
[9] A. Zhou, W. Cheng, W. Wang, Q. Zhao, J. Xie, W. Zhang, H. Gao, L. Xue, J. Li, *Adv. Energy Mater.* **2021**, *11*, 2000943.
[10] K. Hurlbutt, S. Wheeler, I. Capone, M. Pasta, *Joule* **2018**, *2*, 1950.
[11] A. Mullaliu, J. Asenbauer, G. Aquilanti, S. Passerini, M. Giorgetti, *Small Methods* **2020**, *4*, 1900529.
[12] A. Mullaliu, P. Conti, G. Aquilanti, J. Plaisier, L. Stievano, M. Giorgetti, *Condens. Matter* **2018**, *3*, 36.
[13] M. Li, R. Sciacca, M. Maisuradze, G. Aquilanti, J. Plaisier, M. Berrettoni, M. Giorgetti, *Electrochim. Acta* **2021**, *400*, 139414.
[14] A. Mullaliu, G. Aquilanti, J. R. Plaisier, M. Giorgetti, *Condens. Matter* **2021**, *6*, 27.
[15] X. Wu, M. Shao, C. Wu, J. Qian, Y. Cao, X. Ai, H. Yang, *ACS Appl. Mater. Interfaces* **2016**, *8*, 23706.
[16] R. Dugas, J. D. Forero-Saboya, A. Ponrouch, *Chem. Mater.* **2019**, *31*, 8613.
[17] N. Imanishi, T. Morikawa, J. Kondo, Y. Takeda, O. Yamamoto, N. Kinugasa, T. Yamagishi, *J. Power Sources* **1999**, *79*, 215.
[18] J. Song, L. Wang, Y. Lu, J. Liu, B. Guo, P. Xiao, J.-J. Lee, X.-Q. Yang, G. Henkelman, J. B. Goodenough, *J. Am. Chem. Soc.* **2015**, *137*, 2658.
[19] X. Wu, W. Deng, J. Qian, Y. Cao, X. Ai, H. Yang, *J. Mater. Chem. A* **2013**, *1*, 10130.
[20] W.-J. Li, S.-L. Chou, J.-Z. Wang, Y.-M. Kang, J.-L. Wang, Y. Liu, Q.-F. Gu, H.-K. Liu, S.-X. Dou, *Chem. Mater.* **2015**, *27*, 1997.
[21] Y. Yang, E. Liu, X. Yan, C. Ma, W. Wen, X.-Z. Liao, Z.-F. Ma, *J. Electrochem. Soc.* **2016**, *163*, A2117-A2123.
[22] Y. Liu, Y. Qiao, W. Zhang, Z. Li, X. Ji, L. Miao, L. Yuan, X. Hu, Y. Huang, *Nano Energy* **2015**, *12*, 386.
[23] Y. You, X. Yu, Y. Yin, K.-W. Nam, Y.-G. Guo, *Nano Res.* **2015**, *8*, 117.
[24] G. A. Tompsett, W. C. Conner, K. S. Yngvesson, *ChemPhysChem* **2006**, *7*, 296.
[25] A. Birrozzi, F. Maroni, R. Raccichini, R. Tossici, R. Marassi, F. Nobili, *J. Power Sources* **2015**, *294*, 248.
[26] A. Birrozzi, R. Raccichini, F. Nobili, M. Marinaro, R. Tossici, R. Marassi, *Electrochim. Acta* **2014**, *137*, 228.
[27] M. Marinaro, M. Mancini, F. Nobili, R. Tossici, L. Damen, R. Marassi, *J. Power Sources* **2013**, *222*, 66.
[28] F. Maroni, R. Raccichini, A. Birrozzi, G. Carbonari, R. Tossici, F. Croce, R. Marassi, F. Nobili, *J. Power Sources* **2014**, *269*, 873.
[29] F. K. Butt, A. S. Bandarenka, *J. Solid State Electrochem.* **2016**, *20*, 2915.
[30] A. Paolella, C. Faure, V. Timoshevskii, S. Marras, G. Bertoni, A. Guerfi, A. Vijh, M. Armand, K. Zaghib, *J. Mater. Chem. A* **2017**, *5*, 18919.
[31] F. S. Hegner, J. R. Galán-Mascarós, N. López, *Inorg. Chem.* **2016**, *55*, 12851.
[32] J. F. de Wet, R. Rolle, *Z. Anorg. Allg. Chem.* **1965**, *336*, 96.
[33] A. L. Patterson, *Phys. Rev.* **1939**, *56*, 978.
[34] W. Wang, Y. Gang, J. Peng, Z. Hu, Z. Yan, W. Lai, Y. Zhu, D. Appadoo, M. Ye, Y. Cao, Q. F. Gu, H. K. Liu, S. X. Dou, S. L. Chou *Adv. Funct. Mater.* **2022**, *32*, 2111727.
[35] A. Kumar, S. M. Yusuf, L. Keller, *Phys. Rev. B* **2005**, *71*.
[36] W. Weppner, R. A. Huggins, *J. Electrochem. Soc.* **1977**, *124*, 1569.
[37] M. Giorgetti, L. Stievano in *X-ray Characterization of Nanostructured Energy Materials by Synchrotron Radiation* (Eds.: M. Khodaei, L. Petaccia), InTech, **2017**.
[38] M. Giorgetti, *ISRN Materials Science* **2013**, *2013*, 1.

[39] M. Giorgetti, L. Guadagnini, D. Tonelli, M. Minicucci, G. Aquilanti, *Phys. Chem. Chem. Phys.* **2012**, *14*, 5527.
[40] T. E. Westre, P. Kennepohl, J. G. DeWitt, B. Hedman, K. O. Hodgson, E. I. Solomon, *J. Am. Chem. Soc.* **1997**, *119*, 6297.
[41] A. Di Cicco, G. Giuli, A. Trapananti, *Synchrotron Radiation Science and Applications*, Springer International Publishing, Cham, **2021**.
[42] B. H. Toby, R. B. von Dreele, *J. Appl. Crystallogr.* **2013**, *46*, 544.
[43] G. Aquilanti, M. Giorgetti, R. Dominko, L. Stievano, I. Arčon, N. Novello, L. Olivi, *J. Phys. D* **2017**, *50*, 74001.
[44] Filipponi, A. Di Cicco, *Phys. Rev. B* **1995**, *52*, 15135–15149.
[45] M. Giorgetti, M. Berrettoni, A. Filipponi, P. J. Kulesza, R. Marassi, *Chem. Phys. Lett.* **1997**, *275*, 108.

Manuscript received: October 26, 2022
Revised manuscript received: February 6, 2023
Version of record online: March 9, 2023